Tailoring the pore architecture and crystalline structure of UiO-66 for the selective adsorption of anionic species in aqueous media

Hugo G Palhares, Alice G Leonel, Rodrigo L Oréfice, Ricardo O Correia, David Riassetto, Michel Langlet, Manuel Houmard, Eduardo H M Nunes

TAILORING THE PORE ARCHITECTURE AND CRYSTALLINE STRUCTURE OF UiO-66 FOR THE SELECTIVE ADSORPTION OF ANIONIC SPECIES IN AQUEOUS MEDIA

Hugo G. Palhares[1,2*], Alice G. Leonel[1], Rodrigo L. Oréfice[1], Ricardo O. Correia[1], David Riassetto[2], Michel Langlet[2], Manuel Houmard[3,4⊥], Eduardo H.M. Nunes[1,4⊗].

(1) Departamento de Engenharia Metalúrgica e de Materiais, Universidade Federal de Minas Gerais, Pampulha, CEP: 31270-901, Belo Horizonte, MG, Brasil.

(2) Universite Grenoble Alpes, CNRS, Grenoble INP (Institute of Engineering Univ. Grenoble Alpes), LMGP, Grenoble, 38000 France

(3) Departamento de Engenharia Química, Universidade Federal de Minas Gerais, Pampulha, CEP: 31270-901, Belo Horizonte, MG, Brasil.

(4) Centro de Tecnologia em Nanomateriais e Grafeno (CTNano), Rua Professor José Vieira de Mendonça, 520 – Engenho Nogueira, Belo Horizonte – MG, CEP: 31310-260, Brasil.

***** hugogpalhares@gmail.com

⊥ mhoumard@ufmg.br

⊗ eduardo.nunes@demet.ufmg.br

ABSTRACT

Micropollutants such as organic dyes and pharmaceuticals have received much attention in recent years due to their harmful effects on humans and wildlife, high stability against natural degradation, and difficult removal in conventional water treatment plants. In this work, we have optimized the adsorption of organic pollutants on UiO-66 metal-organic frameworks by changing some synthesis parameters, which allowed the tuning of their crystal structure and pore architecture. Samples with an extended microporous structure and specific surface areas over 1300 $m^2.g^{-1}$ were prepared by a solvothermal approach, which favored the access of the pollutant molecules to active adsorption sites. The specific surface areas measured in this study are among the highest ever reported for UiO-66. In batch adsorption tests conducted using aqueous solutions containing low initial concentrations (20 $mg.L^{-1}$) of acid orange (AO7), ibuprofen (IBU), and methylene blue (MB), the materials tested in this study exhibited preferential adsorption of the anionic species AO7 (192 $mg.g^{-1}$) and IBU (173 $mg.g^{-1}$), resulting in AO7/MB and IBU/MB selectivities of 9.6 and 8.7, respectively. The primary adsorption mechanism is most likely a combination of electrostatic and Lewis acid-base interactions involving Zr-(-SO_3^-) for AO7 and Zr-(-CO_2^-) for IBU. Subsequent tests with moderately higher concentrations of AO7 (50 $mg.L^{-1}$) showed even higher adsorption capacities, exceeding 340 $mg.g^{-1}$. These results demonstrate that the optimized UiO-66 structure prepared in this study exhibits high-performance adsorption capabilities for the removal of anionic pollutants from aqueous media, thereby expanding the knowledge on the use of Zr-based MOFs for water remediation.

KEYWORDS: Metal-organic frameworks; UiO-66; organic dyes; non-steroidal anti-inflammatory drugs; adsorption.

1. INTRODUCTION

Metal-organic frameworks (MOFs) have received much attention in the past few decades due to their promising application in different fields, including adsorption (Pedro H M Andrade et al., 2022; Liu et al., 2021b; Madumo et al., 2023; Oladoye et al., 2021; Zango et al., 2021), gas separation/storage (Basu et al., 2011; Hu et al., 2014; Ren et al., 2014; Xie et al., 2018), membrane separation (Deng et al., 2021; Fang et al., 2020), sensing (Koo et al., 2019; Li et al., 2022), drug delivery (Della Rocca et al., 2011; Gordon et al., 2015), and catalysis (Pedro H. M. Andrade et al., 2022; Du et al., 2020; Liu et al., 2023; Man et al., 2022; Rao et al., 2023; Rimoldi et al., 2017). The success of these materials lies in their unique advantages, including very high porosity and specific surface area, controllable pore size, tunable pore surface, and low density (Cao et al., 2021; Furukawa et al., 2010; Oladoye et al., 2021; Zhou et al., 2012). These materials have a highly interconnected three-dimensional pore structure, resulting in specific surface areas of up to several thousand $m^2.g^{-1}$ (Farha et al., 2012). They can be constructed from two counterparts, namely secondary building units (SBUs) and linkers (Tranchemontagne et al., 2009). SBUs are inorganic clusters containing one or more metal ions coordinated by oxygen or nitrogen and connected by linkers (Butova et al., 2021). MOFs can be easily modified by incorporating chemical groups into their structure and changing their surface chemistry. Among the promising applications of MOFs, adsorption deserves to be highlighted. Contaminants such as organic dyes, pharmaceuticals, and personal care products have attracted considerable attention in recent years due to their harmful effects

on humans and wildlife, their high stability against natural degradation, and the difficulty of removal in conventional water treatment plants (Drumond Chequer et al., 2013; Lin et al., 2018; Rozada et al., 2003).

Several strategies have been used for treating wastewaters contaminated with organic pollutants, including ozonation (Wang and Chen, 2020), electrochemical oxidation (Martínez-Huitle and Panizza, 2018), photocatalysis (Gonçalves et al., 2019; Palhares et al., 2020), filtration (Isawi, 2019; Lin et al., 2023), and adsorption (Dey et al., 2019; Lin et al., 2023). Among these, adsorption has been considered a promising approach for removing these and other pollutants due to its low environmental impact, ease of operation, low cost, and high efficiency (Huang et al., 2022; Liu et al., 2021a, 2021b; Wang et al., 2018).

The use of tetravalent metals and dicarboxylate ligands in MOFs is a relatively recent development. First reported in 2008, UiO-66 is a zirconium-based MOF with cubic symmetry and a three-dimensional pore system (Butova et al., 2019; Cavka et al., 2008). This material is known for its good thermal and chemical stability, allowing it to withstand adverse conditions without compromising its structural integrity. Although this MOF has been tested in different applications, such works are generally based on standard routes and barely investigate the influence of synthesis conditions on the structure and properties of the prepared materials (Bambalaza et al., 2018; Bi et al., 2022; Castarlenas et al., 2017; Chen et al., 2017; Dinh et al., 2021; Embaby et al., 2018; Li et al., 2020; Nagarjun et al., 2021; Zhang et al., 2020, 1998). As far as we know, only a few works have evaluated to some extent the influence of the synthesis route on the structure and adsorption behavior of UiO-66 (Cao et al., 2021; Jrad et al., 2022; Qiu et al., 2017; Zhang

et al., 2017). Furthermore, only a few synthesis conditions were evaluated in these studies, indicating the need for additional research to fully understand the structural parameters that impact the adsorption behavior of this MOF. Therefore, this study contributes to a better understanding of the correlation between the synthesis conditions, structure and adsorption properties of UiO-66-based materials. We show here that depending on the type and concentration of the additive used, as well as the relative amount of solvent, structures with different types and degrees of defects can be produced, resulting in different adsorption properties towards anionic and cationic molecules.

In this work, we investigated the structure and adsorption behavior of UiO-66 samples prepared by a facile solvothermal route. The synthesis conditions were varied aiming to obtain specimens with different structures and properties. Organic pollutants such as dyes (acid orange 7, AO7, and methylene blue, MB) and a non-steroidal anti-inflammatory drug (ibuprofen, IBU) were used in the adsorption tests. As mentioned earlier, these are contaminants of great concern in recent years. The Lagergren kinetic model was employed for evaluating the adsorption behavior of the tested samples. These materials were examined by X-ray powder diffraction (XRD), N_2 sorption, thermogravimetry (TG), and transmission electron microscopy (TEM).

2. MATERIALS AND METHODS

The following materials were used in this study as received and without further purification: zirconium tetrachloride ($ZrCl_4$ / Aldrich / ≥ 99.5%), terephthalic acid (H_2BDC / Aldrich / 98%), N,N-Dimethylformamide (DMF / Exodo / ≥ 99.8%), hydrochloric acid (HCl / Vetec / 37%), glacial acetic acid (HAc / Synth / ≥ 99.7%),

absolute ethanol (EtOH / Synth / ≥ 99.5%), and deionized Milli-Q water. For the adsorption tests, acid orange 7 (AO7 / Sigma-Aldrich), methylene blue (MB / Synth), and ibuprofen (IBU / Florien Pharmaceutical Supplies, Brazil) were used as the pollutants.

2.1 MOF SYNTHESIS

The UiO-66 samples were synthesized using a modified protocol of the standard procedure described by Cavka *et al.* (Cavka et al., 2008). Typically, $ZrCl_4$ (1.6 mmol) and H_2BDC (1.6 mmol) were initially mixed with DMF (40 mL). $ZrCl_4$, H_2BDC, and DMF acted as the metal precursor, organic linker, and solvent, respectively. H_2O, HCl, or HAc solutions (40 mL of DMF) were subsequently added to the previously prepared solution. The effect of these additives on the structural properties and adsorption behavior of the prepared MOFs was investigated. The additive/Zr molar ratio was adjusted between 0 and 150. To avoid overly acidic solutions and minimize the influence of large amounts of water added to the reaction media, the molar ratio of additive/Zr was limited to 33 when HCl (37 wt%) was used. The as-obtained solutions were poured into a Teflon-lined stainless-steel autoclave and kept at 120 °C for 24 h. After cooling to room temperature, the obtained crystalline material was washed twice with DMF and then with EtOH. This powder was subsequently sonicated for 30 min in EtOH (50 mL) before drying and finally activated in air at 100 °C. The prepared materials were designated as UiO-66 (X_Y), where X is associated with the additive/linker molar ratio and Y corresponds to the additive used (H_2O, HCl, or HAc). For reference purposes, an additive-free sample was prepared and referred to as UiO-66. In addition, another reference sample was synthesized by reproducing the methodology described by Katz *et al.* (Katz et al., 2013), here designated as UiO-66 (22_HCl_Katz) due to the HCl/Zr molar ratio used. This synthesis method has become a standard in many other studies because it has been shown to

produce MOFs with high specific surface areas (about 1580 $m^2.g^{-1}$) and high adsorption capacity (Katz et al., 2013; Zhang et al., 2017).

Samples were also obtained by increasing the concentration of metal precursor and organic linker relative to the solvent content by a factor of five, resulting in higher yields and more uniform crystal size. In this case, 8.0 mmol of $ZrCl_4$ and 8.0 mmol of H_2BDC were initially mixed with 40 mL of DMF. The synthesis procedure used to prepare these specimens is similar to that reported before. Samples obtained by this method were labeled with the term "5×". As discussed later, the addition of water provided an optimal compromise between desirable structural properties, adsorption behavior, and feasibility. For this reason, these samples were obtained using H_2O as the additive. In these highly concentrated reaction media, another Zr-based MOF could be obtained in the absence of an additive, namely MIL-140A (Guillerm et al., 2012); it has been reported that this framework forms a monoclinic phase with a one-dimensional pore system (Butova et al., 2019; Guillerm et al., 2012).

2.2 CHARACTERIZATIONS

X-ray powder diffraction (XRD) was conducted on a Philips-PANalytical PW1710 diffractometer at a scan rate of $0.03°.s^{-1}$, using CuK_α as the radiation source (λ = 1.54 Å). N_2 sorption tests were conducted at -196°C on a BELSORP-max analyzer using samples outgassed under vacuum at 100 °C for 12 h. The specific surface area (SSA) was evaluated by the multipoint BET (Brunauer-Emmett-Teller) model following the consistency criteria (Ambroz et al., 2018; Guillerm et al., 2012). The non-local density functional theory (NLDFT) and Barrett-Joyner-Halenda (BJH) method were employed to evaluate

the pore size distribution of the examined materials. The microporosity and mesoporosity fractions of the tested samples were evaluated from Eq. (1) and (2), where V_{micro}, V_{meso}, and V_{total} represent, respectively, the micropore, mesopore, and total pore volumes ($cm^3.g^{-1}$).

$$\text{Microporosity} = \frac{V_{micro}}{V_{total}} \quad (1)$$

$$\text{Mesoporosity} = \frac{V_{meso}}{V_{total}} \quad (2)$$

Thermogravimetry (TG) was performed on an Exstar 7200 thermal analyzer at a heating rate of 10 °C.min^{-1} and under N_2 flow (20 mL.min^{-1}). Transmission electron microscopy (TEM) was conducted on an FEI Tecnai G2-20 SuperTwin microscope at an accelerating voltage of 200 kV. The samples used in these tests were previously dispersed in absolute ethanol and sonicated at room temperature for 5 min. The as-obtained suspensions were dripped on carbon-coated grids (Holey Carbon) and then air-dried at room temperature.

2.3 ADSORPTION TESTS

Batch adsorption tests were carried out at room temperature using aqueous solutions containing AO7, MB, or IBU. The adsorbent loading in these solutions was initially kept constant at 200 mg.L^{-1}, while the concentration of AO7, MB, and IBU was set at 20 mg.L^{-1}, unless otherwise specified. The initial pH of these aqueous solutions was about 5 and remained nearly constant during the adsorption tests. The adsorption behavior of the samples prepared in this study was evaluated using the Lagergren kinetic model. The

pseudo-nth-order kinetic law of Lagergren is expressed in Eq. (3), where k_n represents the rate constant for the nth-order adsorption ($mg.g^{-1}.min^{-1}$), q_e is the uptake capacity at equilibrium ($mg.g^{-1}$), and q_t is the adsorption capacity ($mg.g^{-1}$) at time t (min^{-1}) (Ho and McKay, 1998).

$$\frac{dq_t}{dt} = k_n(q_e - q_t)^n \quad (3)$$

The integration of Eq. (3) from t = 0 and t = t ($q_0 = 0$ and $q_t = q_t$) leads to Eq. (4) for the pseudo-second-order (n = 2) law. This model has been effectively used to describe adsorption systems similar to the one studied in this work (Guo et al., 2015; Li et al., 2018; Lin et al., 2018; Qiu et al., 2017).

$$q_t = \frac{k_2 q_e^2 t}{1 + k_2 q_e t} \quad (4)$$

Aliquots collected from these solutions after the adsorption step were centrifuged at 5000 rpm for 10 min. The particle-free supernatant was then transferred to quartz cuvettes and examined by Ultraviolet-Visible (UV-Vis) spectroscopy on a Shimadzu UV-2600 spectrometer at a resolution of 1 nm. The light absorption at 193 nm, 484 nm, and 664 nm was used as a reference for IBU, AO7, and MB, respectively. The uptake of these pollutants on the prepared adsorbents (q_t – $mg.g^{-1}$) was calculated from Eq. (5), where C_0 and C_t represent the initial concentration ($t_0 = 0$) and concentration at time t ($mg.L^{-1}$), V is the solution volume (L), and m is the adsorbent mass (g). The removal efficiency (R – %) was determined from Eq. (6), where C_e represents the concentration at equilibrium (t = t_e).

$$q_t = (C_0 - C_t)\frac{V}{m} \quad (5)$$

$$R = \left(\frac{C_0 - C_e}{C_0}\right) \times 100 \quad (6)$$

3. RESULTS AND DISCUSSION

3.1 INFLUENCE OF H_2O, HCl, HAc ADDITIVES

- STRUCTURAL CHARACTERIZATION

The XRD patterns and TEM micrographs obtained for UiO-66 samples are shown in Fig. 1 and 2. The XRD pattern of the UiO-66 reference and the other samples show a high degree of similarity, indicating that these materials have similar crystalline structures. UiO-66 has particles in the size range of 120-180 nm according to TEM images. In general, the higher the amount of H_2O used, the smaller the particle size of the prepared sample; UiO-66 (10_H_2O), UiO-66 (50_H_2O), and UiO-66 (150_H_2O) have particles in the range of 30-50 nm, 15-25 nm, and 8-12 nm, respectively. This behavior is related to the fast nucleation rate of $Zr_6O_4(OH)_4$ clusters (SBUs) when high concentrations of H_2O are used, which favors the formation of the UiO-66 framework (Ragon et al., 2014; Schaate et al., 2011). On the one hand, the addition of HCl up to 11 eq. decreased the particle size of the prepared MOF; this behavior can also be observed from the broadening of the XRD peak at $2\theta \approx 7.3°$ when UiO-66 (2.2_HCl) and UiO-66 (11_HCl) are compared to UiO-66. On the other hand, further additions of this acid caused a dramatic increase in particle size. This seemingly contradictory behavior may be due to the

combined effect of the pH decrease and the presence of water in the HCl solution (37 wt.% purity). At low pH, the nucleation rate of UiO-66 is slowed down because the deprotonation of H_2BDC (pK_a = 3.54) is inhibited (Ding et al., 2019). However, as discussed earlier, the addition of water has the opposite effect, favoring the nucleation of metal clusters. Thus, HCl has a variable effect on the crystallite size of the prepared MOFs depending on the concentration used. This controversial behavior of HCl has also been discussed elsewhere (Ragon et al., 2014). The addition of either H_2O or HCl caused a loss of the octahedral shape commonly observed for UiO-66 crystals (Fig. 2b-2e). The same behavior was not observed for HAc and the addition of this modulator up to 150 eq. resulted in large octahedral crystals of about 415 nm in size (Fig. 2f). Similar behavior has also been reported in other studies (Bueken et al., 2017; Ragon et al., 2014; Schaate et al., 2011). The peak marked with an asterisk in the XRD patterns displayed in Fig. 1c is associated with a minor phase of unknown origin observed in the HAc-derived samples.

Table 1 brings the textural properties obtained in the N_2 sorption tests (Fig. S1). UiO-66 has a microporous structure (microporosity = 0.9), SSA = 948 $m^2.g^{-1}$, and V_{total} = 0.41 $cm^3.g^{-1}$. These values are in agreement with those described elsewhere (Guillerm et al., 2012; Hao et al., 2018). As a general trend, the use of the different additives slightly expanded the typical micropore structure of the UiO-66 framework and increased the mesopore volume (see NLDFT and BJH in Fig. S1). It can be observed that the use of H_2O was more effective in creating mesoporosity, which can be related to the formation of smaller crystals as discussed previously. This can be clearly seen by the formation of hysteresis loops in the sorption isotherms and BJH distribution. The use of H_2O at 10 eq. caused a dramatic increase in SSA to 1255 $m^2.g^{-1}$ and V_{total} to 0.64 $cm^3.g^{-1}$. These structural changes were accompanied by an increase in the mesoporosity from 0.10 to

0.22. Further additions of H_2O at 50 eq. or 150 eq. caused an increase in mesoporosity fraction to about 0.8, but a decrease in SSA to 831 $m^2.g^{-1}$ and 782 $m^2.g^{-1}$. The higher mesoporosity of UiO-66 (50_H_2O) and UiO-66 (150_H_2O) compared to UiO-66 and UiO-66 (10_H_2O) can also be observed in the N_2 sorption isotherms (Fig. S1), as evidenced by wider hysteresis loops. It has been reported that the hysteresis loop is due to the capillary condensation of N_2 in mesopores (Thommes et al., 2015). This increase in mesoporosity was accompanied by an increase in V_{total} to 1.42 $cm^3.g^{-1}$ and 0.90 $cm^3.g^{-1}$, respectively. The use of HAc and HCl at 10 eq. and 11 eq., respectively, decreased the microporosity of UiO-66 from 0.90 to 0.80. Nonetheless, further additions of these acids increase the microporosity and SSA of this MOF, reaching values above 1300 $m^2.g^{-1}$.

From the results described so far, it can be observed that the preparation of UiO-66 MOFs with small crystallites leads to samples with low microporosity and lower SSA. On the other hand, specimens with large crystallites also have high SSA. This trend was observed for all the additives used in this study. For instance, adding only 10 eq. of H_2O leads to samples with about 40 nm crystal size and 1255 $m^2.g^{-1}$. Increasing this concentration to 50 eq. or 150 eq. results in the formation of materials with crystallites of 20 nm and 10 nm, respectively. The resulting samples have SSA of 831 $m^2.g^{-1}$ and 782 $m^2.g^{-1}$, respectively. In the case of HCl and HAc, a higher amount of additive results in an increased SSA. The high SSA of UiO-66 (22_HCl_Katz) has been assigned to the presence of defects related to missing linkers in the MOF structure; Katz *et al.* (Katz et al., 2013) estimated that about 1/3 of the linkers are missing in this material. The same reasoning can be applied when water is used as an additive, where hydroxyl groups and Cl^- from the $ZrCl_4$ precursor can partially replace the BDC linkers (Shearer et al., 2014). Achieving high SSA requires the controlled formation of defects while maintaining the

integrity of the framework. However, the use of large amounts of water is not effective for this purpose. Finally, it has been argued that the high SSA obtained with the addition of HAc is more likely related to missing cluster defects (Shearer et al., 2016).

- ADSORPTION TESTS

AO7 was initially used as a contaminant in adsorption tests on UiO-66 samples prepared with various additives. The pH remained stable at about 5 and no significant changes were observed throughout the experiments. Table 2 summarizes the evaluated adsorption rate (k_2) and uptake capacity (q_e) based on the adsorption curves obtained (Fig. S2). It can be observed that the pseudo-second-order kinetic model fitted well to the experimental data, displaying a goodness-of-fit (R^2) close to 1. In general, the use of H_2O, HCl, or HAc had a positive effect on the adsorption behavior of UiO-66. As mentioned before, these additives can cause the formation of defects such as missing linkers and missing clusters in the MOF structure, which in turn can increase the total pore volume and improve the adsorption performance. As it can be noticed, such an improvement was not observed for UiO-66 (150_HAc) because this material showed a lower uptake capacity than UiO-66 (51.8 $mg.g^{-1}$ vs. 80.2 $mg.g^{-1}$), despite having faster adsorption kinetics (1.18 $mg.g^{-1}.min^{-1}$ vs. 0.54 $mg.g^{-1}.min^{-1}$). This result could be considered unexpected since UiO-66 (150_HAc) is the sample with the highest SSA among those obtained in this work (1356 $m^2.g^{-1}$). However, as mentioned earlier, the use of HAc is often associated with the presence of missing cluster defects in the MOF structure. According to Zhang *et al.* (Zhang et al., 2017), zirconium ions act as open active sites and can coordinate with the sulfonate groups contained in AO7 through Lewis acid-base interactions. Therefore, the decrease in adsorption capacity observed in samples prepared with higher amounts of

HAc can be attributed to the presence of missing Zr clusters, leading to a reduced number of active sites available for AO7 adsorption.

Zeta potential and thermogravimetric (TG) tests were performed on selected samples (Fig. S3) to validate the adsorption mechanisms. The results were consistent with the previous observation, indicating that the use of HAc is more likely to be associated with the generation of missing cluster defects in the UiO-66 structure than with missing linker defects. On the other hand, the use of H_2O and HCl at 10 eq. and 33 eq. caused a lack of linkers in the MOF framework, which positively affected their adsorption behavior due to the presence of open active sites. In the UiO-66/AO7 system, it was observed that higher positive zeta potentials did not always correlate with increased adsorption of the anionic AO7, contrary to what might have been expected. Again, it was expected that UiO-66 (150_HAc) would have the highest adsorption capacity, but this was not observed. Thus, both the TG and zeta potential results confirm that the primary adsorption mechanism is based on more specific interactions than just electrostatic interactions. In this case, AO7 coordinates with the readily accessible Zr-cluster, facilitated by the presence of missing linker defects, through Lewis acid-base interactions (Zhang et al., 2017).

The most promising adsorption behavior was observed for samples prepared with either low amounts of H_2O (up to 50 eq.) or high additions of HCl (above 11 eq.). In both cases, the pollutant was nearly completely removed from the solution after 180 min of adsorption. UiO-66 (10_H_2O) and UiO-66 (33_HCl) were able to remove about 95% of AO7 in the first 60 min of adsorption. Among the samples prepared with H_2O, it is worth highlighting that UiO-66 (50_H_2O) had faster adsorption kinetics than UiO-66 (10_H_2O)

(5.27×10^{-3} $mg.g^{-1}.min^{-1}$ vs. 2.47×10^{-3} $mg.g^{-1}.min^{-1}$), even though the latter exhibited a higher adsorption capacity (96.3 $mg.g^{-1}$ vs. 101 $mg.g^{-1}$). This result may be due to the large difference in the pore structure of these samples (Table 1). The pore volume and mesoporosity assessed for UiO-66 (10_H_2O) and UiO-66 (50_H_2O) were 0.64 $cm^3.g^{-1}$ and 1.42 $cm^3.g^{-1}$, 0.22 and 0.80, respectively (Table 1). On the other hand, UiO-66 (10_H_2O) displayed a higher SSA (1255 $m^2.g^{-1}$ vs. 831 $m^2.g^{-1}$). These results strongly support the correlation between the adsorption kinetics and the pollutant diffusion within the porous structure of the MOF, which in turn is influenced by the presence of defects. Moreover, the adsorption capacity is influenced not only by the accessibility of the SBUs (which serve as specific sites for the adsorption of anionic species), but also by the abundance of these active sites, which, as previously discussed, is related to both a high specific surface area and the presence of missing linker defects.

3.2 INFLUENCE OF $ZrCl_4$ and H_2BDC CONCENTRATION

- STRUCTURAL CHARACTERIZATION

Fig. 3a shows XRD patterns of samples prepared with a 5-fold increase in metal precursor and organic linker concentration relative to the solvent amount. The XRD patterns of MIL-140A and UiO-66 are also shown for comparison purposes. Although UiO-66 and MIL-140A have similar XRD patterns, the latter has its main peaks shifted to larger 2θ values (Butova et al., 2020). The coexistence of these MOFs in MIL-140A can be noted in Fig. 3b, in which rectangular plates characteristic of the former and octahedral crystals typical of the latter are observed (Butova et al., 2020). The addition of H_2O led to specimens in which UiO-66 is the only phase present. As already observed, increasing

the water concentration decreases the particle size of the prepared MOF (Fig. 3c to 3e). This behavior can also be observed in the XRD patterns displayed in Fig. 3a, where the broadening of the main peak at $2\theta \approx 7.3°$ occurs with increasing the water concentration. The addition of H_2O at concentrations up to 10 eq. led to samples with well-resolved XRD patterns, while further increases in this concentration resulted in specimens with poorly-resolved peaks. Once again, water appears to play a key role in the crystallization of UiO-66.

Fig. 4 shows the N_2 sorption isotherms and NLDFT pore size distributions of the samples prepared after increasing the concentration of $ZrCl_4$ and H_2BDC. Table 3 summarizes the textural parameters obtained from these tests. The theoretical SSA calculated by other authors for MIL-140A and UiO-66 were 360 $m^2.g^{-1}$ and 1125 $m^2.g^{-1}$, respectively (Butova et al., 2020). The values obtained in this work were 597 $m^2.g^{-1}$ and 948 $m^2.g^{-1}$. This difference can be due to the presence of structural defects in these samples, in addition to the existence of additional phases in the MIL-140A sample (Fig. 3a and 3b). The addition up to 10 eq. of water increased the microporosity of the prepared samples (Table 3) and shifted their pore size distribution to larger sizes (Fig. 4b). As a result, UiO-66 (5_H_2O) (5×) and UiO-66 (10_H_2O) (5×) displayed SSA of 1280 $m^2.g^{-1}$ and 1241 $m^2.g^{-1}$, respectively. The use of water at higher concentrations (i.e., 50 eq. or 150 eq.) resulted in samples with higher mesoporosities (up to 0.78) but much lower SSA (as low as 567 $m^2.g^{-1}$). From Fig. 4b it can also be seen that the micropores, which are the typical tetrahedral and octahedral cages, are enlarged for all water-synthesized samples compared to the standard UiO-66. In particular, the UiO-66 (5_H_2O) (5×) sample exhibited the most significant expansion of the tetrahedral cage, leading to enhanced accessibility of the

SBUs to AO7 molecules.. This behavior is discussed in more detail in the following sections.

- ADSORPTION OF AO7

The adsorption behavior of the samples prepared with a high concentration of precursors is summarized in Table 4 (Fig. S4). MIL-140A had a lower uptake capacity (q_e) than UiO-66, which can be related to its smaller micropores, SSA, and V_{total} of the former compared to the latter (597 $m^2.g^{-1}$ vs. 948 $m^2.g^{-1}$, and 0.31 $cm^3.g^{-1}$ vs. 0.41 $cm^3.g^{-1}$). This could result in fewer adsorption sites on the MIL-140A surface, which could reduce its adsorption performance. Regarding the UiO-66 materials obtained with water, their adsorption behavior is positively influenced by increasing the precursor concentration as long as the water addition is maintained up to 10 equivalents. UiO-66 (5_H_2O) (5×) was the sample with the best adsorption performance, displaying a much higher adsorption rate (0.078 $g.mg^{-1}.min^{-1}$). This material was able to remove 97% of AO7 after 5 min of adsorption, and 99% after 15 min. It is worth recalling that this MOF exhibited a very high SSA (1280 $m^2.g^{-1}$) and the largest expansion of the tetrahedral cage to about 1.1 nm (Fig. 4b), which was attributed to the presence of missing linker defects. Considering the dimensions of the AO7 molecule (1.57×1.00×0.54 nm^3) (Zhao et al., 2013), also shown in Fig. S4), it can be inferred that the observed expansion allows the longitudinal access of the dye molecules into the small cages. This in turn not only increases the mobility of the organic molecules within the microporous structure, but also increases the number of accessible adsorption sites (based on Lewis acid-base interactions). The combination of both features explains the high adsorption efficiency of the sample UiO-66 (5_H_2O) (5×). Besides, it showed a well-resolved XRD pattern with sharp peaks (Fig. 3a), which

suggests that it has a highly crystalline structure. The same trend was not observed for UiO-66 (50_H_2O) (5×) and UiO-66 (150_H_2O) (5×). These samples had a sharp decrease in SSA, which is consistent with their poor adsorption performance.

Since UiO-66 (5_H_2O) (5×) showed the most promising adsorption behavior, additional tests were performed with this sample. In these tests, the concentration of adsorbent in the starting solution was systematically varied, from 50 $mg.L^{-1}$ to 200 $mg.L^{-1}$ (Table 5 and Fig. S5). Additionally, the dye concentration was increased from 20 $mg.L^{-1}$ to 50 $mg.L^{-1}$. When used at a concentration of 50 $mg.L^{-1}$, UiO-66 (5_H2O) (5×) showed an outstanding adsorption capacity of more than 300 $mg.g^{-1}$ after only 60 min. Notably, this performance exceeds that of previously reported studies, especially under similar test conditions (Yoon et al., 2019; Zhang et al., 2017).

3.3 SELECTIVE ADSORPTION OF ANIONIC SPECIES

Several studies have suggested that these organic contaminants are adsorbed onto the MOF's surface through a combination of hydrophobic, π-π, electrostatic, and hydrogen bonding interactions (Cao et al., 2021; Chen et al., 2017; Oladoye et al., 2021; Panda et al., 2020). To further investigate the main adsorption mechanism of UiO-66 (5_H_2O) (5×), it was used in adsorption tests conducted with aqueous solutions containing AO7, MB, and IBU. UiO-66 was also employed in these tests for comparison purposes. Both MB and AO7 are organic dyes with comparable molecular sizes of 1.63×0.79×0.40 nm^3 and 1.57×1.00×0.54 nm^3, respectively (Zhao et al., 2013). Moreover, MB is cationic while AO7 is anionic. IBU, a non-steroidal anti-inflammatory drug, is a compound of significant global concern (Rahman and Aziz, 2022). It is anionic and has molecular

448 dimensions significantly smaller than those of AO7 and MB (IBU = 1.03 × 0.52 ×
449 0.43 nm^3 (Mestre et al., 2007)). Fig. 5 shows the adsorption behavior of UiO-66 and
450 UiO-66 (5_H_2O) (5×) as well as the structure of the different molecules tested. It can be
451 seen that the adsorption of both anionic species IBU and AO7 was greater on
452 UiO-66 (5_H_2O) (5×) compared to UiO-66, following the same trend previously
453 observed for AO7 (Table 4). However, an opposite behavior was observed for the cationic
454 MB. UiO-66 (5_H_2O) (5×) showed AO7/MB and IBU/MB selectivities of 9.6 and 8.7,
455 respectively, indicating a greater preference for AO7 and IBU adsorption over MB. These
456 selectivities are much higher compared to those obtained for UiO-66 (2.2 and 2.6,
457 respectively).
458
459 The adsorption of MB was much less pronounced compared to AO7 and IBU, suggesting
460 that electrostatic interactions may also play an important role in the adsorption
461 mechanism of these pollutants on UiO-66 when comparing oppositely charged species.
462 Figure 6 depicts the zeta potential as a function of pH for UiO-66 and UiO-66 (5_H_2O)
463 (5×). The zeta potential of these materials at pH 5 is positive and equal to 10 ± 4 mV
464 (UiO-66) and 15 ± 10 mV (UiO-66 (5_H_2O) (5×)). While the adsorption mechanism of
465 different samples cannot be fully explained by the surface charge alone, as discussed in
466 the previous section (3.1 - Adsorption Tests), the consideration of the opposite charges
467 can certainly help to justify the observed adsorption differences. The positively charged
468 surface of the MOF initiates an electrostatic interaction with the guest molecules,
469 resulting in the repulsion of cationic molecules such as MB, while favoring the
470 penetration of anionic molecules such as AO7 and IBU into the microporous network.
471 Subsequently, more specific interactions can occur leading to the increased adsorption

capacity of anionic species as discussed above. Therefore, the greater surface positivity of UiO-66 (5_H_2O) (5×) contributes to its higher selectivity compared to UiO-66.

As discussed earlier, the porous structure plays a key role in the adsorption process by favoring the diffusion of target molecules into the adsorbent's pore structure, threreby accelerating the adsorption process. This behavior occurs for both anionic (AO7 and IBU) and cationic (MB) species, as evidenced by the increased kinetic rate constants observed for UiO-66 (5_H_2O) (5×) (Fig. 5c), which has an optimized porous structure when compared to that of UiO-66. Also, the adsorption behavior of UiO-66 and UiO-66 (5_H_2O) (5×) was different concerning the anionic pollutants; while the adsorption rate and uptake capacity of UiO-66 is higher when using IBU, the opposite is observed for UiO-66 (5_H_2O) (5×) with AO7 being more adsorbed. UiO-66 exhibited higher adsorption affinity for IBU, which can be attributed to the greater accessibility of IBU to the active adsorption sites due to its smaller molecular size compared to AO7. On the other hand, because UiO-66 (5_H_2O) (5×) has larger micropores, this effect is less pronounced. In fact, its adsorption capacity is even higher for AO7, although the accessibility of IBU is still higher, as suggested by its size and confirmed by the faster kinetic constant. However, it is important to note that when these values are converted to molar capacity, the adsorption capacity of UiO-66 (5_H_2O) (5×) would be 0.59 $mmol.g^{-1}$ for AO7 and 0.84 $mmol.g^{-1}$ for IBU. The values obtained are more representative because adsorption occurs at a finite number of active sites. In this case, both kinetics and adsorption capacity would be higher for IBU compared to AO7. The adsorption differences suggested here are schematically displayed in the inset of Fig. 6.

The adsorption capacities of various adsorbents, including similar MOF structures such as UiO-66 isostructures, are shown in Table 6. It can be observed that the optimized sample, UiO-66 (5_H_2O) (5x), exhibits an excellent adsorption capacity towards anionic pollutants even at relatively low pollutant concentrations at equilibrium (up to 33 ppm). The only other studies that reported similar or higher adsorption capacities used pollutant concentrations much higher than those used here, which was beyond the scope of this investigation. Our optimized material shows not only a significant improvement in adsorption capacity, but also a remarkable increase in adsorption selectivity. The selective adsorption of AO7/MB increased from 2.2 to 9.6 compared to regular UiO-66, indicating a more than 4-fold increase in selectivity.

4. CONCLUSION

We have shown that both crystallinity and porous structure play an important role in the adsorption capacity of organic pollutants on the UiO-66 framework. It was observed that as the SSA and crystallinity increased, the number of active sites for adsorption also increased, resulting in higher adsorption capacity. The intrinsic microporous channels of the framework were also found to be critical in facilitating the access of the adsorbate to the active sites. An optimal number of defects, in the form of missing linkers, resulted in expanded micropore structures with increased specific surface area and exposed cationic Zr active sites. As a result, materials with higher adsoption capacity and faster kinetics could be obtained. The samples that best combined these two properties were obtained using small amounts of water (i.e., 5 eq. or 10 eq.) in a highly concentrated reaction medium. Loading capacities of up to 341 $mg.g^{-1}$ for AO7 and 173 $mg.g^{-1}$ for IBU were achieved at relatively low pollutant concentrations, which are significantly higher

compared to other reports. In addition to the incredibly high adsorption capacity for anionic species, the optimized UiO-66 framework showed outstanding selectivity for the separation of anionic and cationic species, which can be associated with the expanded micropore structure and the increased zeta potential. The main adsorption mechanism involves an initial electrostatic interaction that repels cationic species and restricts their interaction to a few sites on the surface, while allowing anionic species to interact throughout the micropore structure. Subsequently, such anionic molecules can interact more specifically with the defective Zr cluster through Lewis acid-base interactions involving Zr-(-SO_3^-) for AO7 and Zr-(-CO_2^-) for IBU. The $AO7^-/MB^+$ adsorption capacity ratio was remarkably high, reaching 9.6, which is more than 4 times higher than that of the UiO-66 reference sample.

ACKNOWLEDGMENTS

This work was supported by FAPEMIG (APQ-00792-17), CNPq (306193/2020-5, 403191/2021-1, and 304415/2021-9) and CAPES (PROEX / 001). The authors are grateful for the technical support from Centro de Microscopia/UFMG and CTNano.

REFERENCES

Ambroz, F., Macdonald, T.J., Martis, V., Parkin, I.P., 2018. Evaluation of the BET theory for the characterization of meso and microporous MOFs. Small Methods 2, 1800173. https://doi.org/10.1002/smtd.201800173

Andrade, Pedro H. M., Gomes, A.L.M., Palhares, H.G., Volkringer, C., Moissette, A., Victória, H.F. V., Hatem, N.M.A., Krambrock, K., Houmard, M., Nunes, E.H.M., 2022. Post-synthetic modification of aluminum trimesate and copper trimesate with TiO2 nanoparticles for photocatalytic applications. J. Mater. Sci. 57, 4481–4503. https://doi.org/10.1007/s10853-021-06842-w

Andrade, Pedro H M, Henry, N., Volkringer, C., Loiseau, T., Vezin, H., Hureau, M., Moissette, A., 2022. Iodine Uptake by Zr-/Hf-Based UiO-66 Materials: The Influence of Metal Substitution on Iodine Evolution. ACS Appl. Mater. Interfaces 14, 29916–29933. https://doi.org/10.1021/acsami.2c07288

Bambalaza, S.E., Langmi, H.W., Mokaya, R., Musyoka, N.M., Ren, J., Khotseng, L.E., 2018. Compaction of a zirconium metal-organic framework (UiO-66) for high density hydrogen storage applications. J. Mater. Chem. A 6, 23569–23577. https://doi.org/10.1039/C8TA09227C

Basu, S., Cano-Odena, A., Vankelecom, I.F.J., 2011. MOF-containing mixed-matrix membranes for CO2/CH4 and CO2/N2 binary gas mixture separations. Sep. Purif. Technol. 81, 31–40. https://doi.org/10.1016/J.SEPPUR.2011.06.037

Bi, F., Zhao, Z., Yang, Y., Liu, Q., Huang, W., Huang, Y., Zhang, X., 2022. Efficient degradation of toluene over ultra-low Pd supported on UiO-66 and its functional materials: Reaction mechanism, water-resistance, and influence of SO2. Environ. Funct. Mater. 1, 166–181. https://doi.org/10.1016/j.efmat.2022.07.002

Brião, G. V., Jahn, S.L., Foletto, E.L., Dotto, G.L., 2018. Highly efficient and reusable mesoporous zeolite synthetized from a biopolymer for cationic dyes adsorption. Colloids Surfaces A Physicochem. Eng. Asp. 556, 43–50. https://doi.org/10.1016/j.colsurfa.2018.08.019

Bueken, B., Van Velthoven, N., Willhammar, T., Stassin, T., Stassen, I., Keen, D.A.,

570 Baron, G. V., Denayer, J.F.M., Ameloot, R., Bals, S., De Vos, D., Bennett, T.D.,
571 2017. Gel-based morphological design of zirconium metal-organic frameworks.
572 Chem. Sci. 8, 3939–3948. https://doi.org/10.1039/c6sc05602d

573 Butova, V. V., Budnyk, A.P., Charykov, K.M., Vetlitsyna-Novikova, K.S., Lamberti,
574 C., Soldatov, A. V., 2019. Water as a structure-driving agent between the UiO-66
575 and MIL-140A metal-organic frameworks. Chem. Commun. 55, 901–904.
576 https://doi.org/10.1039/c8cc07709f

577 Butova, V. V., Vetlitsyna-Novikova, K.S., Pankin, I.A., Charykov, K.M., Trigub, A.L.,
578 Soldatov, A. V., 2020. Microwave synthesis and phase transition in UiO-66/MIL-
579 140A system. Microporous Mesoporous Mater. 296, 109998.
580 https://doi.org/10.1016/J.MICROMESO.2020.109998

581 Butova, V. V, Pankin, I.A., Burachevskaya, O.A., Vetlitsyna-Novikova, K.S., Soldatov,
582 A. V, 2021. New fast synthesis of MOF-801 for water and hydrogen storage:
583 Modulator effect and recycling options. Inorganica Chim. Acta 514, 120025.
584 https://doi.org/10.1016/j.ica.2020.120025

585 Cao, Y., Chen, X., Li, X., Wang, B., 2021. Tuning Surface Functionalization and Pore
586 Structure of UiO-66 Metal–Organic Framework Nanoparticles for Organic
587 Pollutant Elimination. ACS Appl. Nano Mater. 4, 5486–5495.
588 https://doi.org/10.1021/ACSANM.1C00796

589 Castarlenas, S., Téllez, C., Coronas, J., 2017. Gas separation with mixed matrix
590 membranes obtained from MOF UiO-66-graphite oxide hybrids. J. Memb. Sci.
591 526, 205–211. https://doi.org/10.1016/j.memsci.2016.12.041

592 Cavka, J.H., Jakobsen, S., Olsbye, U., Guillou, N., Lamberti, C., Bordiga, S., Lillerud,
593 K.P., 2008. A New Zirconium Inorganic Building Brick Forming Metal Organic
594 Frameworks with Exceptional Stability. J. Am. Chem. Soc. 130, 13850–13851.
595 https://doi.org/10.1021/ja8057953

596 Chen, C., Chen, D., Xie, S., Quan, H., Luo, X., Guo, L., 2017. Adsorption Behaviors of
597 Organic Micropollutants on Zirconium Metal-Organic Framework UiO-66:
598 Analysis of Surface Interactions. ACS Appl. Mater. Interfaces 9, 41043–41054.
599 https://doi.org/10.1021/acsami.7b13443

600 Della Rocca, J., Liu, D., Lin, W., 2011. Nanoscale metal-organic frameworks for

biomedical imaging and drug delivery. Acc. Chem. Res. 44, 957–68. https://doi.org/10.1021/ar200028a

Deng, Y., Wu, Y., Chen, G., Zheng, X., Dai, M., Peng, C., 2021. Metal-organic framework membranes: Recent development in the synthesis strategies and their application in oil-water separation. Chem. Eng. J. 405, 127004. https://doi.org/10.1016/j.cej.2020.127004

Dey, D., Chandra Murmu, N., Banerjee, P., 2019. Tailor-made synthesis of an melamine-based aminal hydrophobic polymer for selective adsorption of toxic organic pollutants: An initiative towards wastewater purification. RSC Adv. 9, 7469–7478. https://doi.org/10.1039/c9ra00453j

Ding, M., Cai, X., Jiang, H.-L., 2019. Improving MOF stability: approaches and applications. Chem. Sci. 10, 10209–10230. https://doi.org/10.1039/C9SC03916C

Dinh, H.T., Tran, N.T., Trinh, D.X., 2021. Investigation into the Adsorption of Methylene Blue and Methyl Orange by UiO-66-NO2 Nanoparticles. J. Anal. Methods Chem. 2021, 1–10. https://doi.org/10.1155/2021/5512174

Drumond Chequer, F.M., de Oliveira, G.A.R., Anastacio Ferraz, E.R., Carvalho, J., Boldrin Zanoni, M.V., de Oliveir, D.P., 2013. Textile Dyes: Dyeing Process and Environmental Impact, in: Günay, M. (Ed.), Eco-Friendly Textile Dyeing and Finishing. InTech. https://doi.org/10.5772/53659

Du, Q., Wu, P., Sun, Y., Zhang, J., He, H., 2020. Selective photodegradation of tetracycline by molecularly imprinted ZnO@NH2-UiO-66 composites. Chem. Eng. J. 390, 124614. https://doi.org/10.1016/J.CEJ.2020.124614

Embaby, M.S., Elwany, S.D., Setyaningsih, W., Saber, M.R., 2018. The adsorptive properties of UiO-66 towards organic dyes: A record adsorption capacity for the anionic dye Alizarin Red S. Chinese J. Chem. Eng. 26, 731–739. https://doi.org/10.1016/J.CJCHE.2017.07.014

Fang, S.-Y., Zhang, P., Gong, J.-L., Tang, L., Zeng, G.-M., Song, B., Cao, W.-C., Li, J., Ye, J., 2020. Construction of highly water-stable metal-organic framework UiO-66 thin-film composite membrane for dyes and antibiotics separation. Chem. Eng. J. 385, 123400. https://doi.org/10.1016/j.cej.2019.123400

631 Farha, O.K., Eryazici, I., Jeong, N.C., Hauser, B.G., Wilmer, C.E., Sarjeant, A.A.,
632 Snurr, R.Q., Nguyen, S.T., Yazaydın, A.Ö., Hupp, J.T., 2012. Metal–Organic
633 Framework Materials with Ultrahigh Surface Areas: Is the Sky the Limit? J. Am.
634 Chem. Soc. 134, 15016–15021. https://doi.org/10.1021/ja3055639

635 Furukawa, H., Ko, N., Go, Y.B., Aratani, N., Choi, S.B., Choi, E., Yazaydin, A.Ö.,
636 Snurr, R.Q., O'Keeffe, M., Kim, J., Yaghi, O.M., 2010. Ultrahigh Porosity in
637 Metal-Organic Frameworks. Science (80-.). 329, 424–428.
638 https://doi.org/10.1126/science.1192160

639 Gomes, A.L.M., Andrade, P.H.M., Palhares, H.G., Dumont, M.R., Soares, D.C.F.,
640 Volkringer, C., Houmard, M., Nunes, E.H.M., 2021. Facile sol–gel synthesis of
641 silica sorbents for the removal of organic pollutants from aqueous media. J. Mater.
642 Res. Technol. 15, 4580–4594. https://doi.org/10.1016/J.JMRT.2021.10.069

643 Gonçalves, B.S., Palhares, H.G., Souza, T.C.C.D., Castro, V.G.D., Silva, G.G., Silva,
644 B.C., Krambrock, K., Soares, R.B., Lins, V.F.C., Houmard, M., Nunes, E.H.M.,
645 2019. Effect of the carbon loading on the structural and photocatalytic properties of
646 reduced graphene oxide-TiO2 nanocomposites prepared by hydrothermal
647 synthesis. J. Mater. Res. Technol. 8, 6262–6274.
648 https://doi.org/10.1016/j.jmrt.2019.10.020

649 Gordon, J., Kazemian, H., Rohani, S., 2015. MIL-53(Fe), MIL-101, and SBA-15 porous
650 materials: Potential platforms for drug delivery. Mater. Sci. Eng. C 47, 172–179.
651 https://doi.org/10.1016/J.MSEC.2014.11.046

652 Guillerm, V., Ragon, F., Dan-Hardi, M., Devic, T., Vishnuvarthan, M., Campo, B.,
653 Vimont, A., Clet, G., Yang, Q., Maurin, G., Férey, G., Vittadini, A., Gross, S.,
654 Serre, C., 2012. A series of isoreticular, highly stable, porous zirconium oxide
655 based metal-organic frameworks. Angew. Chemie - Int. Ed. 51, 9267–9271.
656 https://doi.org/10.1002/anie.201204806

657 Guo, H., Lin, F., Chen, J., Li, F., Weng, W., 2015. Metal-organic framework MIL-
658 125(Ti) for efficient adsorptive removal of Rhodamine B from aqueous solution.
659 Appl. Organomet. Chem. 29, 12–19. https://doi.org/10.1002/aoc.3237

660 Hao, L., Li, X., Hurlock, M.J., Tu, X., Zhang, Q., 2018. Hierarchically porous UiO-66:
661 Facile synthesis, characterization and application. Chem. Commun. 54, 11817–

11820. https://doi.org/10.1039/c8cc05895d

Ho, Y.S., McKay, G., 1998. A Comparison of chemisorption kinetic models applied to pollutant removal on various sorbents. Process Saf. Environ. Prot. 76, 332–340. https://doi.org/10.1205/095758298529696

Hu, Y., Verdegaal, W.M., Yu, S.H., Jiang, H.L., 2014. Alkylamine-tethered stable metal-organic framework for CO2 capture from flue gas. ChemSusChem 7, 734–737. https://doi.org/10.1002/cssc.201301163

Huang, L., Cao, H., Ma, J., Wang, X., 2022. Efficient removal of Pb(II) by UiO-66-NH2: A combined experimental and spectroscopic studies. Environ. Nanotechnology, Monit. Manag. 18, 100741. https://doi.org/10.1016/j.enmm.2022.100741

Isawi, H., 2019. Evaluating the performance of different nano-enhanced ultrafiltration membranes for the removal of organic pollutants from wastewater. J. Water Process Eng. 31, 100833. https://doi.org/10.1016/j.jwpe.2019.100833

Jrad, A., Damacet, P., Yaghi, Z., Ahmad, M., Hmadeh, M., 2022. Zr-Based Metal–Organic Framework Nanocrystals for Water Remediation. ACS Appl. Nano Mater. 5, 10795–10808. https://doi.org/10.1021/acsanm.2c02128

Katz, M.J., Brown, Z.J., Colón, Y.J., Siu, P.W., Scheidt, K.A., Snurr, R.Q., Hupp, J.T., Farha, O.K., 2013. A facile synthesis of UiO-66, UiO-67 and their derivatives. Chem. Commun. 49, 9449. https://doi.org/10.1039/c3cc46105j

Koo, W.-T., Jang, J.-S., Kim, I.-D., 2019. Metal-Organic Frameworks for Chemiresistive Sensors. Chem 5, 1938–1963. https://doi.org/10.1016/J.CHEMPR.2019.04.013

Li, J., Gong, J.L., Zeng, G.M., Zhang, P., Song, B., Cao, W.C., Liu, H.Y., Huan, S.Y., 2018. Zirconium-based metal organic frameworks loaded on polyurethane foam membrane for simultaneous removal of dyes with different charges. J. Colloid Interface Sci. 527, 267–279. https://doi.org/10.1016/J.JCIS.2018.05.028

Li, Y.X., Wang, X., Wang, C.C., Fu, H., Liu, Y., Wang, P., Zhao, C., 2020. S-TiO2/UiO-66-NH2 composite for boosted photocatalytic Cr(VI) reduction and bisphenol A degradation under LED visible light. J. Hazard. Mater. 399, 123085.

https://doi.org/10.1016/J.JHAZMAT.2020.123085

Li, Z., Li, Q., Jiang, R., Qin, Y., Luo, Y., Li, J., Kong, W., Yang, Z., Huang, C., Qu, X., Wang, T., Cui, L., Wang, G., Yang, S., Liu, Z., Guo, X., 2022. An electrochemical sensor based on a MOF/ZnO composite for the highly sensitive detection of Cu(ii) in river water samples. RSC Adv. 12, 5062–5071. https://doi.org/10.1039/D1RA08376G

Lin, H., Jie, B., Ye, J., Zhai, Y., Luo, Z., Shao, G., Chen, R., Zhang, X., Yang, Y., 2023. Recent advance of macroscopic metal-organic frameworks for water treatment: A review. Surfaces and Interfaces 36, 102564. https://doi.org/10.1016/j.surfin.2022.102564

Lin, S., Zhao, Y., Yun, Y.-S., 2018. Highly Effective Removal of Nonsteroidal Anti-inflammatory Pharmaceuticals from Water by Zr(IV)-Based Metal–Organic Framework: Adsorption Performance and Mechanisms. ACS Appl. Mater. Interfaces 10, 28076–28085. https://doi.org/10.1021/ACSAMI.8B08596

Liu, N., Hu, B., Tang, K., Xia, T., Li, F., Quan, G., Zhang, X., Tang, L., 2023. Assembling UiO-66 into layered HTiNbO5 nanosheets for efficient photocatalytic CO2 reduction. Surfaces and Interfaces 41, 103134. https://doi.org/10.1016/j.surfin.2023.103134

Liu, Y., Huo, Y., Wang, Xiangxue, Yu, S., Ai, Y., Chen, Z., Zhang, P., Chen, L., Song, G., Alharbi, N.S., Rabah, S.O., Wang, Xiangke, 2021a. Impact of metal ions and organic ligands on uranium removal properties by zeolitic imidazolate framework materials. J. Clean. Prod. 278, 123216. https://doi.org/10.1016/j.jclepro.2020.123216

Liu, Y., Pang, H., Wang, Xiangxue, Yu, S., Chen, Z., Zhang, P., Chen, L., Song, G., Saleh Alharbi, N., Omar Rabah, S., Wang, Xiangke, 2021b. Zeolitic imidazolate framework-based nanomaterials for the capture of heavy metal ions and radionuclides: A review. Chem. Eng. J. 406, 127139. https://doi.org/10.1016/j.cej.2020.127139

Madumo, T.M., Zikalala, S.A., Gumbi, N.N., Mishra, S.B., Ntsendwana, B., Nxumalo, E.N., 2023. Development of nitrogen-doped graphene/MOF nanocomposites towards adsorptive removal of Cr(VI) from the wastewater of the Herbert Bickley

723 treatment works. Environ. Nanotechnology, Monit. Manag. 20, 100794.
724 https://doi.org/10.1016/j.enmm.2023.100794

725 Man, Z., Meng, Y., Lin, X., Dai, X., Wang, L., Liu, D., 2022. Assembling UiO-
726 66@TiO2 nanocomposites for efficient photocatalytic degradation of dimethyl
727 sulfide. Chem. Eng. J. 431, 133952. https://doi.org/10.1016/J.CEJ.2021.133952

728 Martínez-Huitle, C.A., Panizza, M., 2018. Electrochemical oxidation of organic
729 pollutants for wastewater treatment. Curr. Opin. Electrochem.
730 https://doi.org/10.1016/j.coelec.2018.07.010

731 Mestre, A.S., Pires, J., Nogueira, J.M.F., Carvalho, A.P., 2007. Activated carbons for
732 the adsorption of ibuprofen. Carbon N. Y. 45, 1979–1988.
733 https://doi.org/10.1016/J.CARBON.2007.06.005

734 Nagarjun, N., Jacob, M., Varalakshmi, P., Dhakshinamoorthy, A., 2021. UiO-66(Ce)
735 metal-organic framework as a highly active and selective catalyst for the aerobic
736 oxidation of benzyl amines. Mol. Catal. 499, 111277.
737 https://doi.org/10.1016/j.mcat.2020.111277

738 Oladoye, P.O., Adegboyega, S.A., Giwa, A.R.A., 2021. Remediation potentials of
739 composite metal-organic frameworks (MOFs) for dyes as water contaminants: A
740 comprehensive review of recent literatures. Environ. Nanotechnology, Monit.
741 Manag. 16, 100568. https://doi.org/10.1016/j.enmm.2021.100568

742 Palhares, H.G., Gonçalves, B.S., Silva, L.M.C., Nunes, E.H.M., Houmard, M., 2020.
743 Clarifying the roles of hydrothermal treatment and silica addition to synthesize
744 TiO2-based nanocomposites with high photocatalytic performance. J. Sol-Gel Sci.
745 Technol. 95, 119–135. https://doi.org/10.1007/s10971-020-05265-4

746 Panda, J., Sahu, S.N., Sahoo, J.K., Biswal, S.P., Pattanayak, S.K., Samantaray, R., Sahu,
747 R., 2020. Efficient removal of two anionic dyes by a highly robust zirconium based
748 metal organic framework from aqueous medium: Experimental findings with
749 molecular docking study. Environ. Nanotechnology, Monit. Manag. 14, 100340.
750 https://doi.org/10.1016/j.enmm.2020.100340

751 Qiu, J., Feng, Y., Zhang, X., Jia, M., Yao, J., 2017. Acid-promoted synthesis of UiO-66
752 for highly selective adsorption of anionic dyes: Adsorption performance and
753 mechanisms. J. Colloid Interface Sci. 499, 151–158.

754 https://doi.org/10.1016/J.JCIS.2017.03.101

755 Ragon, F., Horcajada, P., Chevreau, H., Hwang, Y.K., Lee, U.H., Miller, S.R., Devic,
756 T., Chang, J.S., Serre, C., 2014. In situ energy-dispersive x-ray diffraction for the
757 synthesis optimization and scale-up of the porous zirconium terephthalate UiO-66.
758 Inorg. Chem. 53, 2491–2500. https://doi.org/10.1021/ic402514n

759 Rahman, K.O., Aziz, K.H.H., 2022. Utilizing scrap printed circuit boards to fabricate
760 efficient Fenton-like catalysts for the removal of pharmaceutical diclofenac and
761 ibuprofen from water. J. Environ. Chem. Eng. 10, 109015.
762 https://doi.org/10.1016/j.jece.2022.109015

763 Rao, R., Ma, S., Gao, B., Bi, F., Chen, Y., Yang, Y., Liu, N., Wu, M., Zhang, X., 2023.
764 Recent advances of metal-organic framework-based and derivative materials in the
765 heterogeneous catalytic removal of volatile organic compounds. J. Colloid
766 Interface Sci. 636, 55–72. https://doi.org/10.1016/j.jcis.2022.12.167

767 Ren, J., Langmi, H.W., North, B.C., Mathe, M., Bessarabov, D., 2014. Modulated
768 synthesis of zirconium-metal organic framework (Zr-MOF) for hydrogen storage
769 applications. Int. J. Hydrogen Energy 39, 890–895.
770 https://doi.org/10.1016/j.ijhydene.2013.10.087

771 Rimoldi, M., Howarth, A.J., Destefano, M.R., Lin, L., Goswami, S., Li, P., Hupp, J.T.,
772 Farha, O.K., 2017. Catalytic Zirconium/Hafnium-Based Metal-Organic
773 Frameworks. ACS Catal. 7, 997–1014. https://doi.org/10.1021/acscatal.6b02923

774 Rozada, F., Calvo, L.F., García, A.I., Martín-Villacorta, J., Otero, M., 2003. Dye
775 adsorption by sewage sludge-based activated carbons in batch and fixed-bed
776 systems. Bioresour. Technol. 87, 221–230. https://doi.org/10.1016/S0960-
777 8524(02)00243-2

778 Schaate, A., Roy, P., Godt, A., Lippke, J., Waltz, F., Wiebcke, M., Behrens, P., 2011.
779 Modulated Synthesis of Zr-Based Metal-Organic Frameworks: From Nano to
780 Single Crystals. Chem. - A Eur. J. 17, 6643–6651.
781 https://doi.org/10.1002/chem.201003211

782 Shearer, G.C., Chavan, S., Bordiga, S., Svelle, S., Olsbye, U., Lillerud, K.P., 2016.
783 Defect Engineering: Tuning the Porosity and Composition of the Metal–Organic
784 Framework UiO-66 via Modulated Synthesis. Chem. Mater. 28, 3749–3761.

https://doi.org/10.1021/acs.chemmater.6b00602

Shearer, G.C., Chavan, S., Ethiraj, J., Vitillo, J.G., Svelle, S., Olsbye, U., Lamberti, C., Bordiga, S., Lillerud, K.P., 2014. Tuned to Perfection: Ironing Out the Defects in Metal–Organic Framework UiO-66. Chem. Mater. 26, 4068–4071. https://doi.org/10.1021/cm501859p

Sun, W., Li, Haibo, Li, Huimin, Li, S., Cao, X., 2019. Adsorption mechanisms of ibuprofen and naproxen to UiO-66 and UiO-66-NH2: Batch experiment and DFT calculation. Chem. Eng. J. 360, 645–653. https://doi.org/10.1016/J.CEJ.2018.12.021

Thommes, M., Kaneko, K., Neimark, A. V., Olivier, J.P., Rodriguez-Reinoso, F., Rouquerol, J., Sing, K.S.W., 2015. Physisorption of gases, with special reference to the evaluation of surface area and pore size distribution (IUPAC Technical Report). Pure Appl. Chem. 87, 1051–1069. https://doi.org/10.1515/pac-2014-1117

Tranchemontagne, D.J., Mendoza-Cortés, J.L., O'Keeffe, M., Yaghi, O.M., 2009. Secondary building units, nets and bonding in the chemistry of metal–organic frameworks. Chem. Soc. Rev. 38, 1257–1283. https://doi.org/10.1039/B817735J

Wang, J., Chen, H., 2020. Catalytic ozonation for water and wastewater treatment: Recent advances and perspective. Sci. Total Environ. 704, 135249. https://doi.org/10.1016/j.scitotenv.2019.135249

Wang, J., Zhao, S. qi, Zhang, M. ya, He, B. shu, 2018. Targeted eco-pharmacovigilance for ketoprofen in the environment: Need, strategy and challenge. Chemosphere. https://doi.org/10.1016/j.chemosphere.2017.12.020

Xie, K., Fu, Q., Xu, C., Lu, H., Zhao, Q., Curtain, R., Gu, D., Webley, P.A., Qiao, G.G., 2018. Continuous assembly of a polymer on a metal–organic framework (CAP on MOF): a 30 nm thick polymeric gas separation membrane. Energy Environ. Sci. 11, 544–550. https://doi.org/10.1039/C7EE02820B

Yang, J.M., 2017. A facile approach to fabricate an immobilized-phosphate zirconium-based metal-organic framework composite (UiO-66-P) and its activity in the adsorption and separation of organic dyes. J. Colloid Interface Sci. 505, 178–185. https://doi.org/10.1016/J.JCIS.2017.05.040

Yoon, S., Calvo, J.J., So, M.C., 2019. Removal of acid orange 7 from aqueous solution by metal-organic frameworks. Crystals 9. https://doi.org/10.3390/cryst9010017

Zango, Z.U., Jumbri, K., Sambudi, N.S., Abu Bakar, H.H., Garba, Z.N., Isiyaka, H.A., Saad, B., 2021. Selective adsorption of dyes and pharmaceuticals from water by UiO metal–organic frameworks: A comprehensive review. Polyhedron 210, 115515. https://doi.org/10.1016/J.POLY.2021.115515

Zhang, J., Hu, Y., Qin, J., Yang, Z., Fu, M., 2020. TiO2-UiO-66-NH2 nanocomposites as efficient photocatalysts for the oxidation of VOCs. Chem. Eng. J. 385, 123814. https://doi.org/10.1016/j.cej.2019.123814

Zhang, K.D., Tsai, F.C., Ma, N., Xia, Y., Liu, H.L., Zhan, X.Q., Yu, X.Y., Zeng, X.Z., Jiang, T., Shi, D., Chang, C.J., 2017. Adsorption behavior of high stable Zr-Based MOFs for the removal of acid organic dye from water. Materials (Basel). 10. https://doi.org/10.3390/MA10020205

Zhang, Z., Wang, C.-C., Zakaria, R., Ying, J.Y., 1998. Role of Particle Size in Nanocrystalline TiO2-Based Photocatalysts. J. Phys. Chem. B 102, 10871–10878. https://doi.org/10.1021/JP982948+

Zhao, D., Cai, C., 2021. Cerium-based UiO-66 metal-organic framework for synergistic dye adsorption and photodegradation: A discussion of the mechanism. Dye. Pigment. 185, 108957. https://doi.org/10.1016/J.DYEPIG.2020.108957

Zhao, X., Bu, X., Wu, T., Zheng, S.T., Wang, L., Feng, P., 2013. Selective anion exchange with nanogated isoreticular positive metal-organic frameworks. Nat. Commun. 2013 41 4, 1–9. https://doi.org/10.1038/ncomms3344

Zhou, H.C., Long, J.R., Yaghi, O.M., 2012. Introduction to metal-organic frameworks. Chem. Rev. 112, 673–674. https://doi.org/10.1021/cr300014x

TABLES

Table 1: Textural properties evaluated from the N_2 sorption.

Sample	SSA ($m^2.g^{-1}$)	V_{micro} ($cm^3.g^{-1}$)	V_{meso} ($cm^3.g^{-1}$)	V_{total} ($cm^3.g^{-1}$)	Micro-porosity (V_{micro}/V_{total})	Meso-porosity (V_{meso}/V_{total})
UiO-66	948	0.37	0.04	0.41	0.90	0.10
UiO-66 (10_H_2O)	1255	0.50	0.14	0.64	0.78	0.22
UiO-66 (50_H_2O)	831	0.28	1.14	1.42	0.20	0.80
UiO-66 (150_H_2O)	782	0.20	0.70	0.90	0.22	0.78
UiO-66 (2.2_HCl)	593	0.23	0.12	0.35	0.66	0.34
UiO-66 (11_HCl)	833	0.33	0.08	0.41	0.80	0.20
UiO-66 (22_HCl_Katz)	1349	0.55	0.10	0.65	0.85	0.15
UiO-66 (33_HCl)	1292	0.51	0.07	0.58	0.88	0.12
UiO-66 (10_HAc)	1223	0.52	0.12	0.64	0.81	0.19
UiO-66 (50_HAc)	1305	0.58	0.12	0.70	0.83	0.17
UiO-66 (150_HAc)	1356	0.56	0.04	0.60	0.93	0.07

Table 2: Summary of AO7 adsorption by various samples using pseudo-second-order kinetics, with the removal efficiency evaluated at 180 min.

Sample	$k_2 \times 10^{-3}$ ($g.mg^{-1}.min^{-1}$)	q_e ($mg.g^{-1}$)	R^2	Removal Efficiency (%)
UiO-66	0.54	80.2	0.97	75
UiO-66 (10_H_2O)	2.47	101.0	1.00	100
UiO-66 (50_H_2O)	5.27	96.3	1.00	97
UiO-66 (150_H_2O)	2.52	95.5	0.99	96
UiO-66 (2.2_HCl)	1.24	76.9	0.99	74
UiO-66 (11_HCl)	2.20	95.6	1.00	95
UiO-66 (22_HCl_Katz)	2.68	102.8	1.00	98
UiO-66 (33_HCl)	3.25	102.6	1.00	98
UiO-66 (10_HAc)	3.72	101.5	0.99	93
UiO-66 (50_HAc)	1.51	98.9	0.96	90
UiO-66 (150_HAc)	1.18	51.8	0.97	51

Table 3: Textural properties of samples prepared using water as an additive at higher concentrations.

Sample	SSA ($m^2.g^{-1}$)	V_{micro} ($cm^3.g^{-1}$)	V_{meso} ($cm^3.g^{-1}$)	V_{total} ($cm^3.g^{-1}$)	Micro-porosity (V_{micro}/V_{total})	Meso-porosity (V_{meso}/V_{total})
UiO-66	948	0.37	0.04	0.41	0.90	0.10
MIL-140A	597	0.24	0.07	0.31	0.77	0.23
UiO-66 (5_H_2O) (5x)	1280	0.49	0.04	0.53	0.92	0.08
UiO-66 (10_H_2O) (5x)	1241	0.47	0.04	0.51	0.92	0.08
UiO-66 (50_H_2O) (5x)	890	0.31	1.11	1.42	0.22	0.78
UiO-66 (150_H_2O) (5x)	567	0.18	0.22	0.40	0.45	0.55

855

856 Table 4: Summary of AO7 adsorption kinetics on samples synthesized with
857 H_2O and a 5-fold increase in precursor concentration, evaluated with pseudo-
858 second-order kinetics, with the removal efficiency measured at 180 min.

Sample	$k_2 \times 10^{-3}$ ($g.mg^{-1}.min^{-1}$)	q_e ($mg.g^{-1}$)	R^2	Removal Efficiency (%)
MIL-140A	1.56	57.8	0.97	58
UiO-66	0.54	80.2	0.97	75
UiO-66 (5_H_2O) (5x)	78.31	102.1	1.00	100
UiO-66 (10_H_2O) (5x)	7.23	100.7	1.00	100
UiO-66 (50_H_2O) (5x)	2.47	80.3	0.99	80
UiO-66 (150_H_2O) (5x)	1.83	61.5	0.98	61

859

860

861

Table 5: Summary of AO7 adsorption kinetics on UiO-66 (5_H2O) (5×) optimized sample at different concentrations, using pseudo-second-order kinetics and measuring removal efficiency at 180 min.

Adsorbent concentration ($mg.L^{-1}$)	**$k_2 \times 10^{-3}$ ($g.mg^{-1}.min^{-1}$)**	**q_e ($mg.g^{-1}$)**	**R^2**	**Removal Efficiency (%)**
50	0.47	341.10	0.99	34
100	0.70	295.10	0.99	59
150	1.21	262.50	1.00	78
200	1.67	230.00	1.00	92

868 Table 6: Comparison of the adsorption performance of the samples prepared
869 in this study and others reported elsewhere.

Adsorbent	**Pollutant**	**Adsorption Condition** C_{eq} in $mg.L^{-1}$	**Adsorption Result** Q_e and Q_{max} in $mg.g^{-1}$ k_2 in $x10^{-3}$ $g.mg^{-1}.min^{-1}$	**Ref.**
UiO-66	AO7 –	-Langmuir isotherm C_{eq} up to 230 (298K) -Kinetics – pseudo 2nd order C_{eq} = 28	-Q_{max} = 332 -Qe = 220 (k_2 = 0.025)	(Zhang et al., 2017)
UiO-66 UiO-66 (NH_2)	AO7 –	-Kinetics – pseudo 2nd order C_{eq} = 39 -Kinetics – pseudo 2nd order C_{eq} = 41	-Q_e = 107 (k_2 = N/S) -Q_e = 85 (k_2 = N/S)	(Yoon et al., 2019)
UiO-66(Ce)	AO7 – MO – MB +	-Langmuir isotherm C_{eq} up to 130 -Langmuir isotherm C_{eq} up to 150 -Langmuir isotherm C_{eq} up to 160	-Q_{max} = 427 -Q_{max} = 298 -Q_{max} = 249	(Zhao and Cai, 2021)
UiO-66	MO – MB +	Langmuir isotherm C_{eq} up to 500	-Q_{max} = 176 -Q_{max} = 22	(Yang, 2017)
UiO-66-P	MO – MB +	Langmuir isotherm C_{eq} up to 500	-Q_{max} = 3.5 -Q_{max} = 95	(Yang, 2017)
UiO-66	MO – MB +	-Kinectics – pseudo 2nd order C_{eq} = 6 -Kinectics – pseudo 2nd order C_{eq} = 7	-Q_e = 70 (k_2 = N/S) -Q_e = 67 (k_2 = N/S)	(Qiu et al., 2017)
UiO-66 (HCl)	MO – MB +	-Kinectics – pseudo 2nd order C_{eq} = 2 -Kinectics – pseudo 2nd order C_{eq} = 17	-Q_e = 85 (k_2 = N/S) -Q_e = 13 (k_2 = N/S)	(Qiu et al., 2017)

UiO-66-NO_2	MB + MO –	-Langmuir isotherm C_{eq} up to 160 -Langmuir isotherm C_{eq} up to 160	Q_{max} = 41.7 Q_{max} = 142.9	(Dinh et al., 2021)
-UiO-66 -D_UiO-66	IBU –	-Kinectics – pseudo 2nd order C_{eq} = 1.8 -Kinectics – pseudo 2nd order C_{eq} = 0.3	Q_e = 73 (k_2 = 11) Q_e = 79 (k_2 = 558)	(Cao et al., 2021)
-UiO-66 -NH_2-UiO-66	IBU –	-Kinectics – pseudo 2nd order C_{eq} = 3 -Kinectics – pseudo 2nd order C_{eq} = 6.5	-Q_e = 128 (k_2 = 0.56) -Q_e = 51 (k_2 = 0.85)	(Sun et al., 2019)
Silica	MB + DIP –	-Kinectics – pseudo 2nd order C_{eq} = 8 -Kinectics – pseudo 2nd order C_{eq} = 79	-Q_e = 37 (k_2 = N/S) -Q_e = 8.5 (k_2 = N/S)	(Gomes et al., 2021)
Activated Carbon CPAC	IBU	-Kinetics – pseudo 2nd order C_{eq} = 0.5	Q_e = 89 (k_2 = 5.2)	(Mestre et al., 2007)
Zeolite	MB + CV +	-Langmuir isotherm C_{eq} up to 135(298K) -Langmuir isotherm C_{eq} up to 185(298K)	Q_{max} = 78 Q_{max} = 86	(Brião et al., 2018)
UiO-66 (5_H_2O) (5x)	AO7	-Kinectics – pseudo 2nd order C_{eq} = 33 -Kinectics – pseudo 2nd order C_{eq} = 20 -Kinectics – pseudo 2nd order C_{eq} = 0.8	-Q_e = 341 (k_2 = 0.5) -Q_e = 295 (k_2 = 0.7) -Q_e = 192 (k_2 = 2.9)	This work
UiO-66 (5_H_2O) (5x)	IBU	Kinetics – pseudo 2nd order C_{eq} = 2.9	Q_e = 173 (k_2 = 4.3)	This work
UiO-66 (5_H_2O) (5x)	MB	Kinetics – pseudo 2nd order C_{eq} = 18	Q_e = 20 (k_2 = 15)	This work

870

871

872

FIGURES

Figure 1

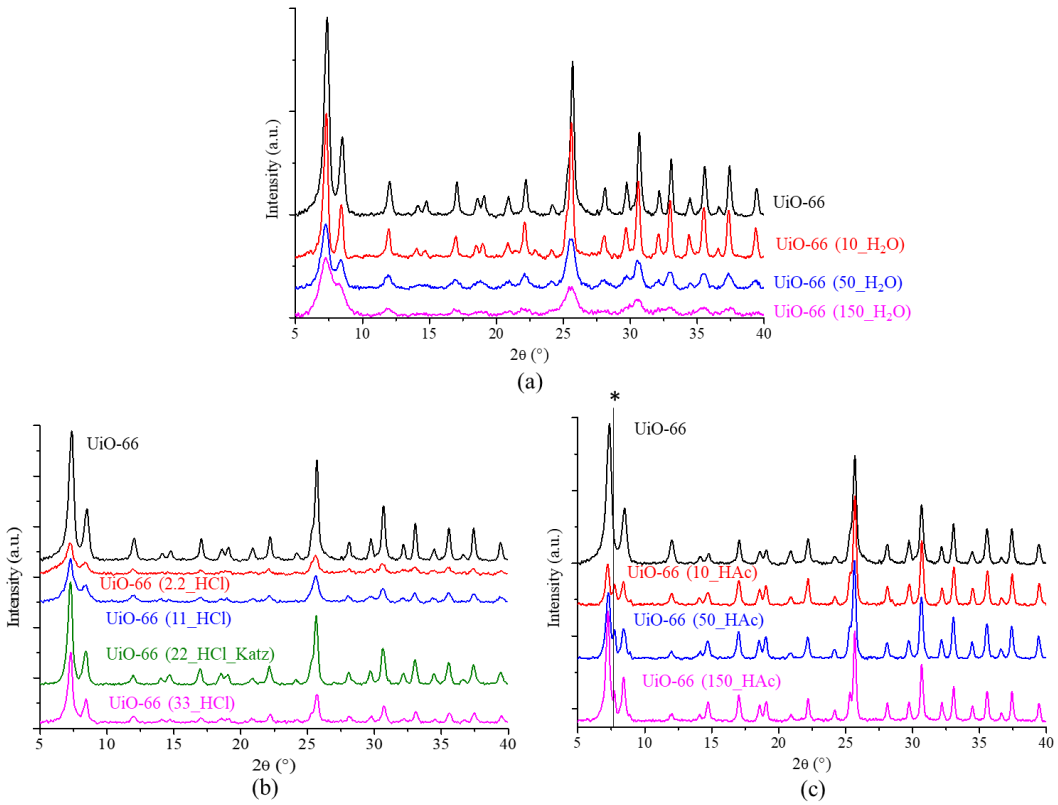

Figure 1: XRD patterns of UiO-66 specimens prepared using (a) H_2O, (b) HCl, and (c) HAc as additives. The peak marked with the symbol "*" is assigned to minor phases observed in the HAc-derived MOFs.

Figure 2

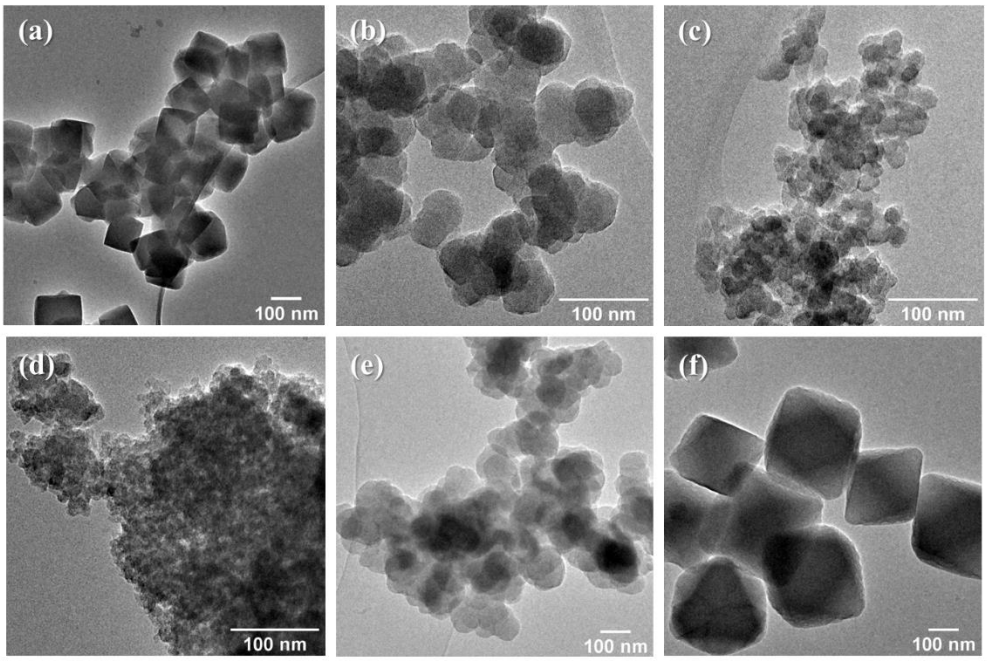

- Figure 2: TEM micrographs of UiO-66 samples obtained in this work. (a) UiO-66, (b) UiO-66 (10_H_2O), (c) UiO-66 (50_H_2O), (d) UiO-66 (150_H_2O), (e) UiO-66 (33_HCl), and (f) UiO-66 (150_HAc).

Figure 3

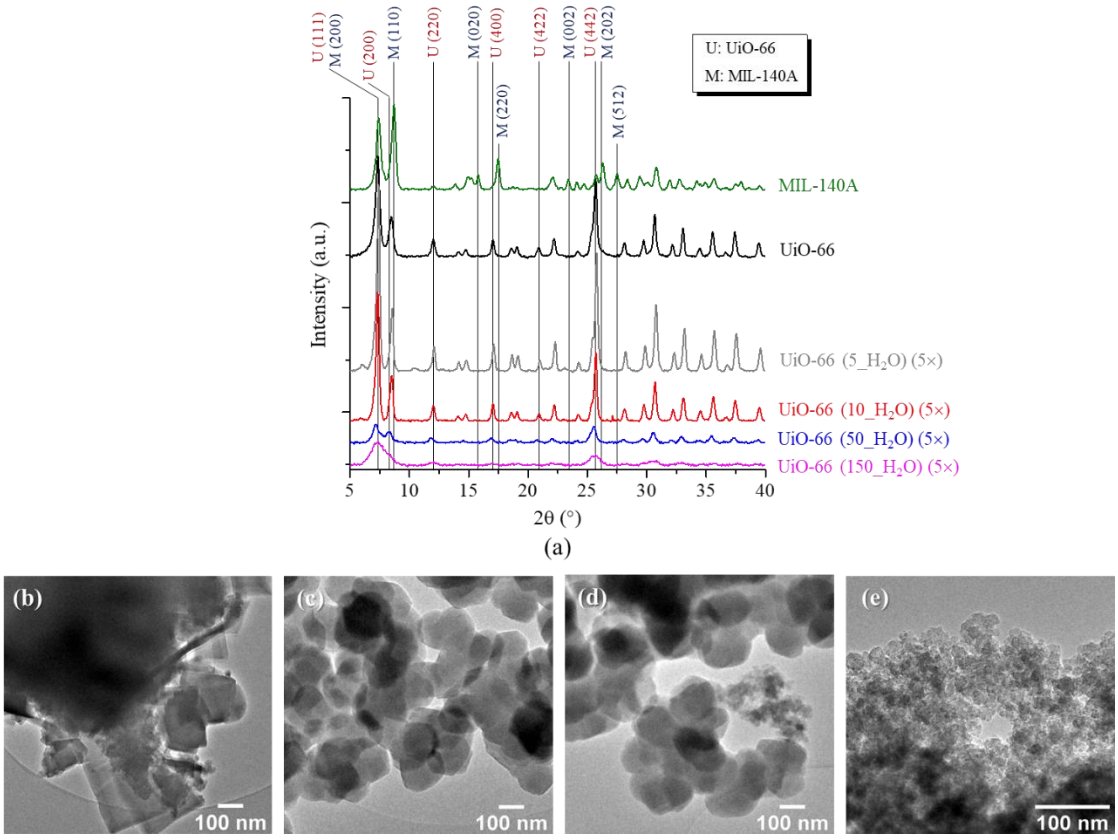

- **Figure 3:** (a) XRD pattern of samples obtained after a 5-fold increase in the concentration of $ZrCl_4$ and H_2BDC. The XRD patterns of UiO-66 and MIL-140A are also displayed for reference purposes. The highlighted diffraction peaks have been indexed according to the work of Butova *et al.* (Butova et al., 2020). TEM micrographs of (b) MIL-140A, (c) UiO-66 (5_H_2O) (5×), (d) UiO-66 (10_H_2O) (5×), and (e) UiO-66 (50_H_2O) (5×) are also exhibited.

Figure 4

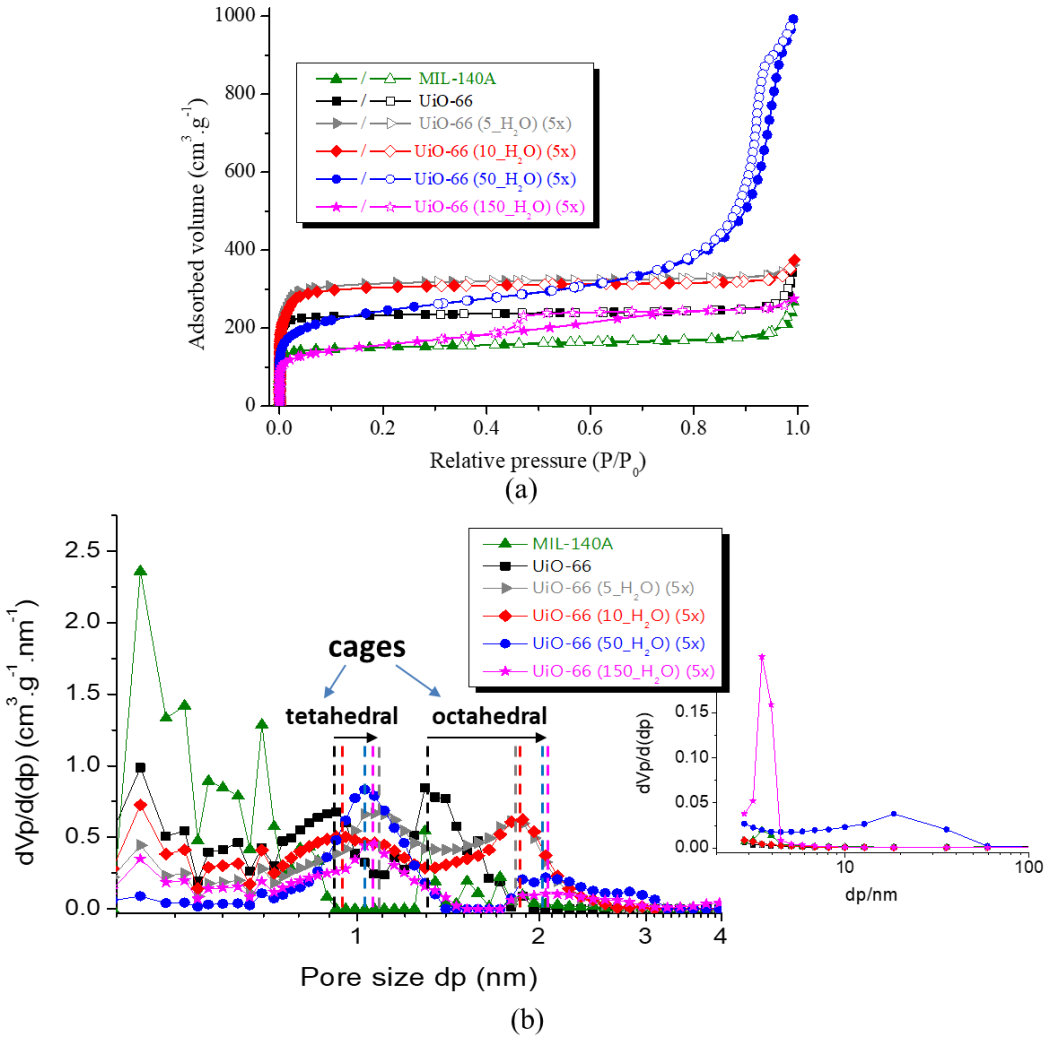

- **Figure 4:** (a) N_2 sorption isotherms and (b) NLDFT and BJH (inset) pore size distributions of samples obtained after a 5-fold increase in the concentration of $ZrCl_4$ and H_2BDC relative to DMF. The closed and open symbols are related to the adsorption and desorption branches, respectively. The data ascribed to UiO-66 and MIL-140A are also depicted for comparison purposes.

Figure 5

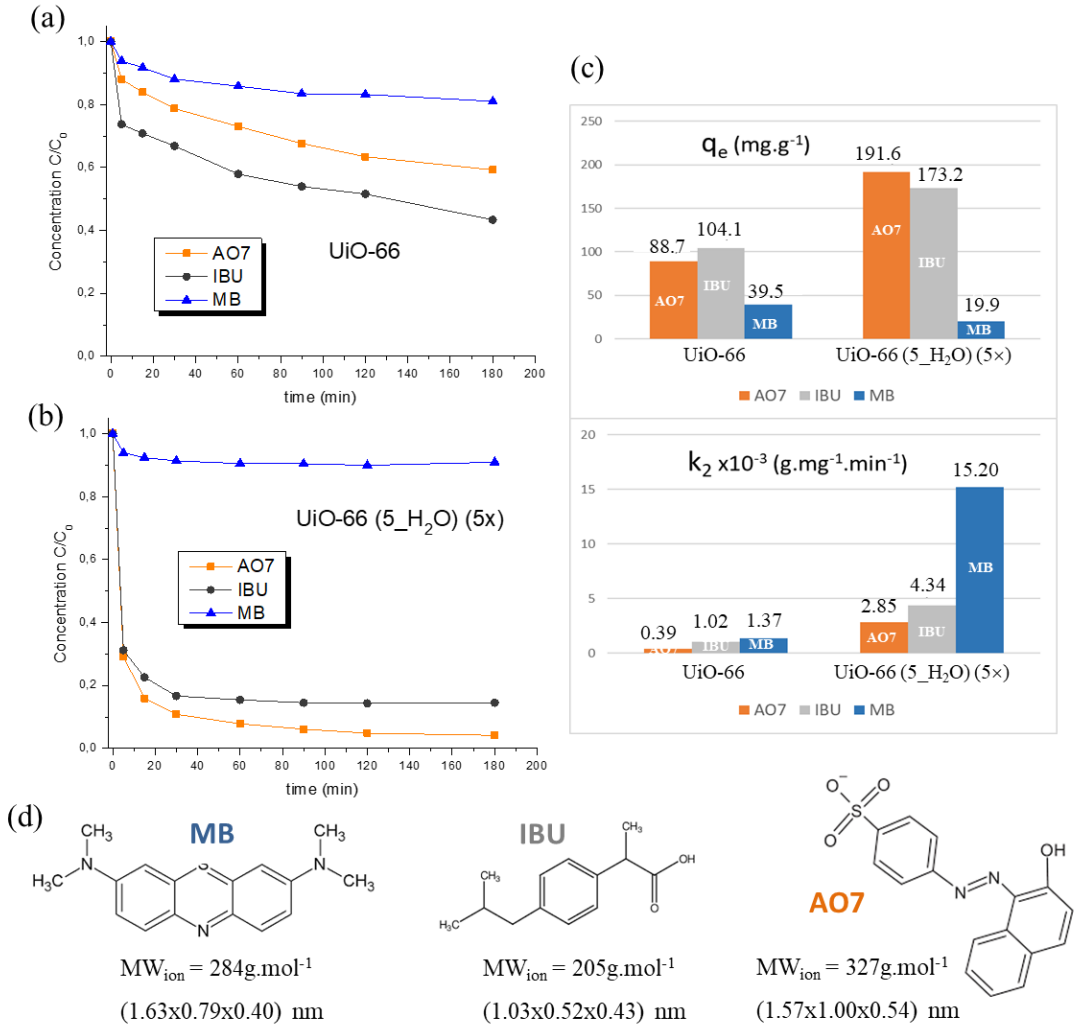

- Figure 5: Adsorption behavior of (a) UiO-66 and (b) UiO-66 (5_H_2O) (5×) in aqueous solutions containing AO7, IBU, and MB. The concentration of adsorbent and pollutants was kept at 100 mg.L^{-1} and 20 mg.L^{-1}, respectively. (c) Comparison of the pseudo-second-order adsorption rate constant (k_2) and uptake capacity at equilibrium (q_e) evaluated for these MOFs. (d) Structural representations of the different pollutants used.

Figure 6

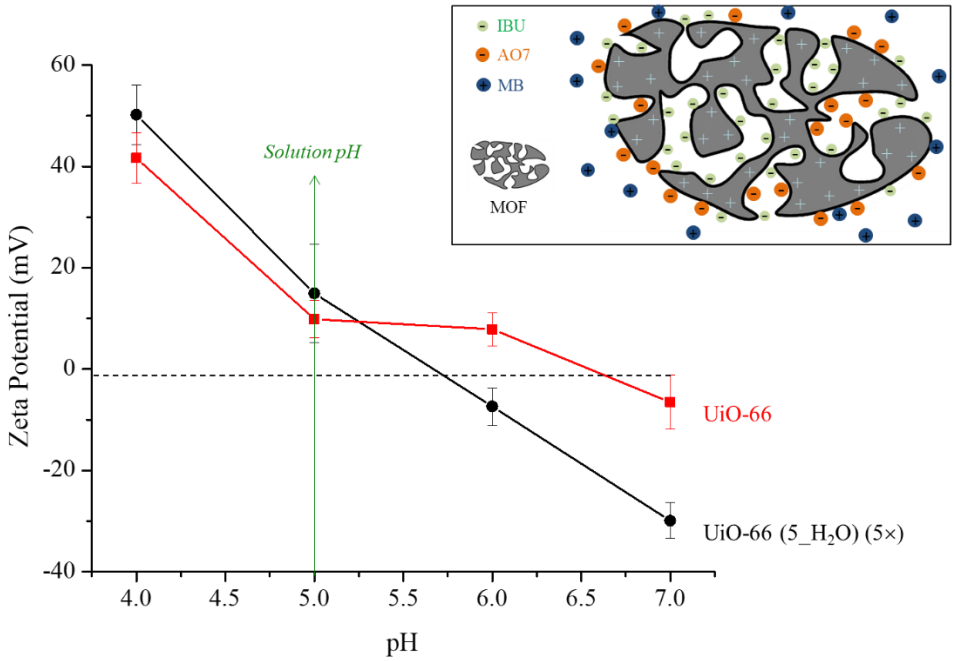

- **Figure 6:** Zeta potential as a function of pH for UiO-66 and UiO-66 (5_H_2O) (5×). Inset: schematic representation comparing the adsorption mechanism of AO7, IBU, and MB on the optimized porous structure of UiO-66 (5_H_2O) (5×).